JURNAL INFOTEL
VOL. 18, NO. 3, AUGUST 2026, PP. 388–410. DOI:10.20895/INFOTEL.V18I3.11124

RESEARCH ARTICLE

Design and Experimental Evaluation of a UV-C Disinfection Robotic Manipulator Integrated with a Mobile Robot Platform

Rama Okta Wiyagi[1,*], Muhamad Yusvin Mustar[2], Tony K. Hariadi[3], Maria Ulfa[4], Arya Adiningrat[5], and Bintang Surya Tryatmojo[6]

[1,2,3,6] Department of Electrical Engineering, Universitas Muhammadiyah Yogyakarta, Indonesia
[4] School of Medicine, Faculty of Medicine and Health Sciences, Universitas Muhammadiyah Yogyakarta, Indonesia
[5] Oral Biology and Biomedical Sciences Department, Faculty of Dentistry, Universitas Muhammadiyah Yogyakarta, Indonesia

*Corresponding email: ramaoktawiyagi@umy.ac.id

Received: May 19, 2026; Revised: August 26, 2026; Accepted: September 12, 2026.

Abstract: This paper presents the design and experimental evaluation of the an ultraviolet C (UV-C) disinfection robotic manipulator integrated with a mobile robot platform for contactless indoor disinfection. The system supports hospital infection-control procedures by enabling remote positioning of UV-C lamps toward shadow-prone surfaces while reducing operator exposure. The manipulator has three degrees of freedom (3-DoF) and is implemented as an articulated arm driven by four linear actuators and equipped with two UV-C lamps near the end-effector. The evaluation covered actuator driver voltage, travel time, joint-angle range, vertical reach, and forward kinematics-based workspace estimation. The driver output voltage decreased from 12.6 V at idle to 12.0–12.2 V during operation, indicating stable power delivery under load. The actuator travel time ranged from 14.70 s to 16.32 s. The measured joint-angle ranges were $20°$–$62°$, $18°$–$62°$, and $38°$–$67°$ for Joints 1–3, respectively, with an end-effector height of 129.5–224 cm. The forward kinematics model estimated a horizontal reach of -76.3–137.9 cm and a vertical workspace of 134.5–220.5 cm. These results indicate that the manipulator can carry and orient dual UV-C lamps across multiple configurations for indoor disinfection. Future work will include UV dose mapping, irradiation uniformity analysis, and microbiological validation.

Keywords: indoor healthcare environment, linear actuator, mobile robot platform, robotic manipulator, tele-operation, UV-C disinfection

© Jurnal Infotel ISSN: 2085-3688; e-ISSN: 2460-0997

1 Introduction

The COVID-19 pandemic highlighted the urgent need for more effective infection prevention and control strategies, particularly in healthcare facilities. Hospitals, as frontline institutions providing comprehensive health services, must ensure that all clinical and support areas are regularly cleaned and disinfected. During the COVID-19 pandemic, this requirement is even more critical, as insufficient or inconsistent disinfection can accelerate the spread of viruses and other pathogenic microorganisms within hospital environments. Beyond routine cleaning, additional efforts are required to inactivate infectious agents on surfaces, particularly in high-risk areas such as emergency rooms, intensive care units, and patient wards.

One of the most commonly implemented strategies to reduce the risk of transmission is social distancing, which aims to minimize physical contact and limit the number of people in a given space. However, the application of social distancing in hospital settings presents practical challenges, particularly during room disinfection procedures that traditionally rely on manual labor. Conventional manual disinfection requires cleaning personnel to enter potentially contaminated spaces, thereby increasing their risk of exposure. At the same time, it is desirable to reduce the number of personnel involved in such activities to comply with social distancing guidelines. These conflicting requirements motivate the exploration of technology-based solutions that can maintain disinfection quality while protecting healthcare workers.

The spraying of disinfectants with liquid chemicals is a common method used in many environments. However, in hospital rooms, the extensive use of liquid disinfectants can be problematic. Sensitive medical instruments, electronic equipment, and various materials used in clinical settings can be damaged or degraded by repeated exposure to chemical agents or excessive moisture. As a result, ultraviolet (UV) irradiation has emerged as an attractive alternative method for environmental disinfection. UV, particularly in the germicidal UV-C range, can inactivate microorganisms on exposed surfaces without leaving chemical residues and with minimal impact on medical equipment when applied correctly. This method makes UV-C-based disinfection highly suitable for hospital environments, provided that the UV-C source can be directed accurately and safely.

Fundamentally, UV radiation behaves like light and therefore follows line-of-sight propagation. When an object obstructs the UV-C beam, it casts a shadow region behind it. Surfaces within this shadowed area receive little or no UV exposure and consequently are not effectively disinfected. In complex hospital rooms filled with beds, monitors, stands, cables, and other equipment, these shadowed regions can be extensive and irregular. If left unaddressed, they may become hotspots for the survival and proliferation of viruses and bacteria. This limitation of static UV-C sources, such as fixed lamps or simple UV towers, motivates the need for a more flexible mechanism capable of directing UV light to complex and hard-to-reach surfaces.

A promising approach to overcome this challenge is the use of a robotic manipulator to control the position and orientation of the UV-C source. By employing a multi-degree-of-freedom robotic arm, the UV-C emitter can be moved intelligently around obstacles, allowing targeted irradiation of surfaces that would otherwise remain in shadow. This approach enables a more thorough and adaptive disinfection, particularly in cluttered or geometrically complex environments. In addition, integrating the manipulator with a mo-

bile base can further extend its operational coverage, resulting in a complete disinfection robot capable of navigating through different rooms and zones in hospital environments.

The present research focuses on the design and development of such a robotic arm as the main mechanism for directing UV light during disinfection tasks. The proposed disinfection robotic arm is conceived as a key subsystem of a larger mobile disinfection robot. When combined with a mobile robot platform, it forms a complete system capable of both navigating and performing targeted UV disinfection. The arm consists of several electric actuators that provide the necessary degrees of freedom to control the direction, angle, and reach of the UV-C source. This configuration enables the system to adapt to various spatial arrangements and systematically cover surfaces prone to shadowing.

Safety considerations are crucial in the design of UV-C-based disinfection systems, as direct exposure to UV radiation can harm human skin and eyes. For this reason, operators should not remain inside the room while disinfection is in progress. To address this issue, the proposed robotic arm is controlled using a wireless interface. The wireless control system allows an operator to monitor and command the arm from outside the disinfected area, thus maintaining a safe distance and eliminating direct exposure during operation. Through remote control, adjustments to the arm's position and orientation can be made in real time to ensure that all critical surfaces receive adequate UV exposure.

In summary, this study aims to develop a UV-C disinfection robotic manipulator capable of directing UV-C irradiation to complex and shadow-prone surfaces in hospital rooms while allowing safe remote operation. The main contribution of this work is the design and implementation of a wireless-controlled, multi-degree-of-freedom robotic arm as a core component of a mobile disinfection robot. The expected outcome of this research is a robotic disinfection manipulator that can support safer and more effective disinfection procedures, reduce exposure risk for healthcare workers, and contribute to improved infection control in hospital environments.

2 Related Work

The COVID-19 pandemic accelerated the deployment of advanced information and automation technologies in healthcare and increased the demand for solutions that enable safer operations under strict infection-control protocols. Within the broader Industry~4.0 paradigm, enabling technologies such as the Internet of Things, cloud-based monitoring, data-driven decision support, and autonomous robotic systems have been identified as important contributors to contactless operation and service continuity in high-risk environments such as hospitals [1].

In parallel with this technological shift, the pandemic triggered wider adoption and discussion of robotic systems for logistics, tele-presence, healthcare assistance, and environmental decontamination. A comprehensive review of real-world COVID-19 robot deployments reported their use across multiple response categories, including cleaning and disinfection [2]. Similarly, a broad survey on robots under the COVID-19 pandemic emphasized disinfection as a major application area in both healthcare and public environments [3]. These studies indicate that robotic systems have become increasingly relevant not only as technical tools, but also as part of redesigned workflows for reducing human exposure in high-risk environments.

Human–Robot Interaction (HRI) research has also recognized that COVID-19 reshaped the operational context of robots, particularly in safety-critical settings. The pandemic shifted HRI priorities toward interaction paradigms that explicitly address physical distancing, hygiene, safety, and user trust under uncertain and high-stress conditions [4]. Beyond interface design, the pandemic also highlighted the need to rethink *human–robot collaborative work* as a means of reducing risks to essential workers, rather than focusing solely on the technical substitution of human labor [5].

Among the robotic applications intensified by COVID-19, disinfection robots have emerged as one of the most important categories. Disinfection platforms generally rely on either chemical agents, such as sprays or aerosolized disinfectants, or ultraviolet (UV) irradiation. Chemical approaches can be effective, but their use in hospital rooms may be constrained by the presence of sensitive medical instruments, electronic devices, and materials that are vulnerable to moisture, residue, or chemical exposure. UV-C-based disinfection, particularly germicidal UV-C irradiation, offers an attractive alternative because it can inactivate microorganisms on exposed surfaces without leaving chemical residues [6]. However, UV-C disinfection is inherently constrained by line-of-sight propagation. Occlusions caused by beds, carts, monitors, furniture, or other objects can create shadowed regions that receive insufficient UV dose and may remain potential reservoirs for pathogens [6].

A substantial body of work has studied mobile robots equipped with UV lamps for indoor disinfection. Conte *et al.* presented a mobile UV-C disinfection robot with map-based tele-operation, combining autonomous navigation with operator supervision to support safer operation in complex indoor environments [7]. Guettari *et al.* experimentally validated the germicidal effectiveness of a UV-C disinfection robot under controlled conditions and demonstrated a significant reduction in microbial load on exposed surfaces [8]. While these systems are effective for broad area treatment, many mobile UV-C robots still use fixed lamp assemblies mounted on the mobile base. Consequently, their disinfection performance may degrade in occluded regions unless the coverage strategy explicitly accounts for shading and line-of-sight limitations.

More recent studies have investigated modeling, planning, and evaluation methods for improving UV-C disinfection robotics. Chio *et al.* introduced an indoor disinfection robot whose navigation and operation are driven by a disinfection modeling framework, emphasizing the integration of task-level disinfection requirements with autonomous motion in indoor spaces [9]. Zaman *et al.* proposed UVC-PURGE, a semi-autonomous UV-C disinfection robot that combines teleoperation support, real-time camera feedback, low-cost hardware design, and experimental validation to improve usability in resource-constrained contexts [10]. These works demonstrate that effective UV-C disinfection requires not only mobile robot deployment, but also an appropriate integration of sensing, navigation, supervision, and disinfection-performance evaluation.

Several IEEE-sponsored studies have further contributed key building blocks for UV-C disinfection robotics. Mikhailovskiy *et al.* presented UltraBot, an autonomous mobile robot for indoor UV-C disinfection, and reported experimental evidence of bacterial-count reduction under indoor irradiation while considering non-trivial disinfection-zone geometry [11]. Marques *et al.* formulated an optimized coverage-planning method for UV surface disinfection by explicitly incorporating dosage constraints and occlusion into trajectory optimization [12]. Conroy *et al.* also investigated robot development and path planning for indoor ultraviolet-light disinfection, targeting improved time efficiency and coverage compared with baseline strategies [13]. Collectively, these studies show that navigation, cover-

age planning, occlusion handling, and dose modeling are central to achieving effective UV disinfection at the room scale.

Recent studies have also emphasized mobile manipulation as a promising approach for addressing the limitations of fixed-lamp UV-C robots. Sanchez and Smart proposed a verifiable UV surface-disinfection approach using a mobile manipulation robot, demonstrating the benefit of positioning the UV source closer to target surfaces and verifying disinfection coverage [14]. Mehta *et al.* developed a far-UVC disinfection system using a robotic mobile manipulator, in which the UV emitter was mounted on a multi-degree-of-freedom arm to treat high-contact surfaces more flexibly [15]. These studies are particularly relevant to the present work because they show that integrating a UV source with a robotic manipulator can improve the ability to treat partially occluded, geometrically complex, or difficult-to-reach surfaces.

In addition to mobile manipulation, recent work has focused on optimizing UV-C disinfection coverage through workspace-aware and path-planning strategies. Zhang *et al.* proposed a joint base placement and multi-configuration path-planning method for 3D surface disinfection with a UV-C robotic system, highlighting the importance of base position, manipulator configuration, and surface coverage in achieving effective irradiation [16]. Guo *et al.* investigated coverage planning for UVC irradiation using a swarm intelligence algorithm, further demonstrating that UV-C disinfection performance depends not only on the robot hardware but also on the planning strategy used to cover the target surface [17]. These studies support the need for workspace estimation and future coverage-planning development in UV-C robotic disinfection systems.

Beyond UV-C-only platforms, other systems have explored chemical or hybrid disinfection modalities. For example, the "Smart Cleaner" robot integrates a mobile base with a hydrogen-peroxide atomization device and reports validation in practical indoor scenarios [18]. Nevertheless, many existing mobile disinfection robots, particularly UV-C-based platforms, still employ fixed lamp geometries mounted on the mobile base. As a result, the achievable disinfection quality remains limited by line-of-sight constraints, especially for complex, occluded, or hard-to-reach surfaces. Although teleoperation and supervised autonomy have been widely discussed for reducing operator exposure [5,7,10], relatively few platforms provide *fine-grained control of UV-C beam direction* through an articulated multi-degree-of-freedom manipulator dedicated to treating shadowed regions.

Recent works by Mustar *et al.* have also addressed robotic subsystems that are relevant to the development of mobile manipulation platforms. Mustar *et al.* designed and implemented a 2-DOF robotic manipulator based on inverse kinematics for an agricultural robotic competition, demonstrating the role of kinematic modeling in task-oriented end-effector positioning [19]. Although the application domain differs from UV-C disinfection, the study provides a relevant reference for manipulator design and kinematics-based workspace analysis. In another study, Mustar *et al.* explored the use of an Intel RealSense T265 camera as a visual odometry and tracking system for autonomous navigation of a four-wheel omnidirectional mobile robot [20]. This work is relevant to the mobile-platform aspect of disinfection robotics, particularly for future development involving autonomous navigation, visual odometry, and coordinated motion between the mobile base and the robotic arm.

The biological effectiveness of UV irradiation and its dependence on source-to-target distance were investigated in our previous study [21]. In that work, several UV sources, including a PHILIPS UV-C Disinfection Desk Lamp, were evaluated using SARS-CoV-2

RNA as representative viral genetic material under different irradiation conditions. The results demonstrated that exposure conditions, particularly irradiation distance and duration, influenced the degradation of viral genetic material. The PHILIPS UV-C desk lamp also degraded the targeted viral genetic material under the evaluated conditions.

These findings provide biological motivation for controlling the relative position between the UV-C source and the target surface. However, the previous study considered directly irradiated samples and did not address geometrical occlusion or shadowing in complex indoor environments. Therefore, the present work focuses on the robotic aspect of the problem by developing an articulated manipulator capable of changing the position and orientation of the UV-C source to improve access to surfaces that cannot be directly irradiated from a fixed lamp position.

Against this background, the present work addresses a specific gap by developing a UV-C disinfection robotic manipulator dedicated to directing UV-C irradiation toward complex and shadow-prone surfaces as part of a broader mobile disinfection system. In contrast to fixed-lamp mobile UV-C robots, the proposed system provides wireless remote operation and controllable arm posture, including direction, angle, reach, and workspace estimation. This approach is intended to reduce operator exposure while improving the ability of the disinfection platform to irradiate occluded surfaces that are difficult to treat using fixed UV-C lamp configurations.

3 System Design

3.1 Overall Architecture

The proposed system is a modular UV-C disinfection robotic manipulator that can be mounted on a mobile robot platform. The system architecture follows a typical teleoperated mechatronic chain: a wireless operator interface serves as the primary input; a central controller processes the received command signals; the controller generates actuator-level commands, which are amplified by high-current motor drivers to drive the arm actuators, as shown in Figure 1. This architecture is reflected in the system diagram, where wireless commands are treated as the primary input, followed by controller processing and power amplification at the driver stage (Figure 2). The manipulator is intended to enable disinfection while keeping the operator outside the irradiated area. The proposed system uses a wirelessly controlled arm that allows the operator to perform disinfection remotely during UV exposure.

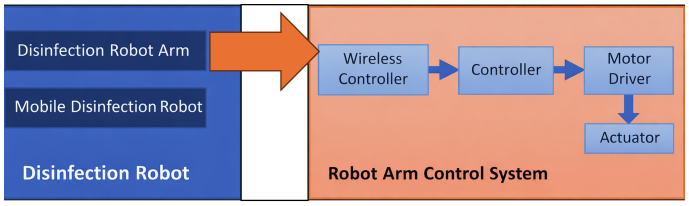

Figure 1: General system block diagram.

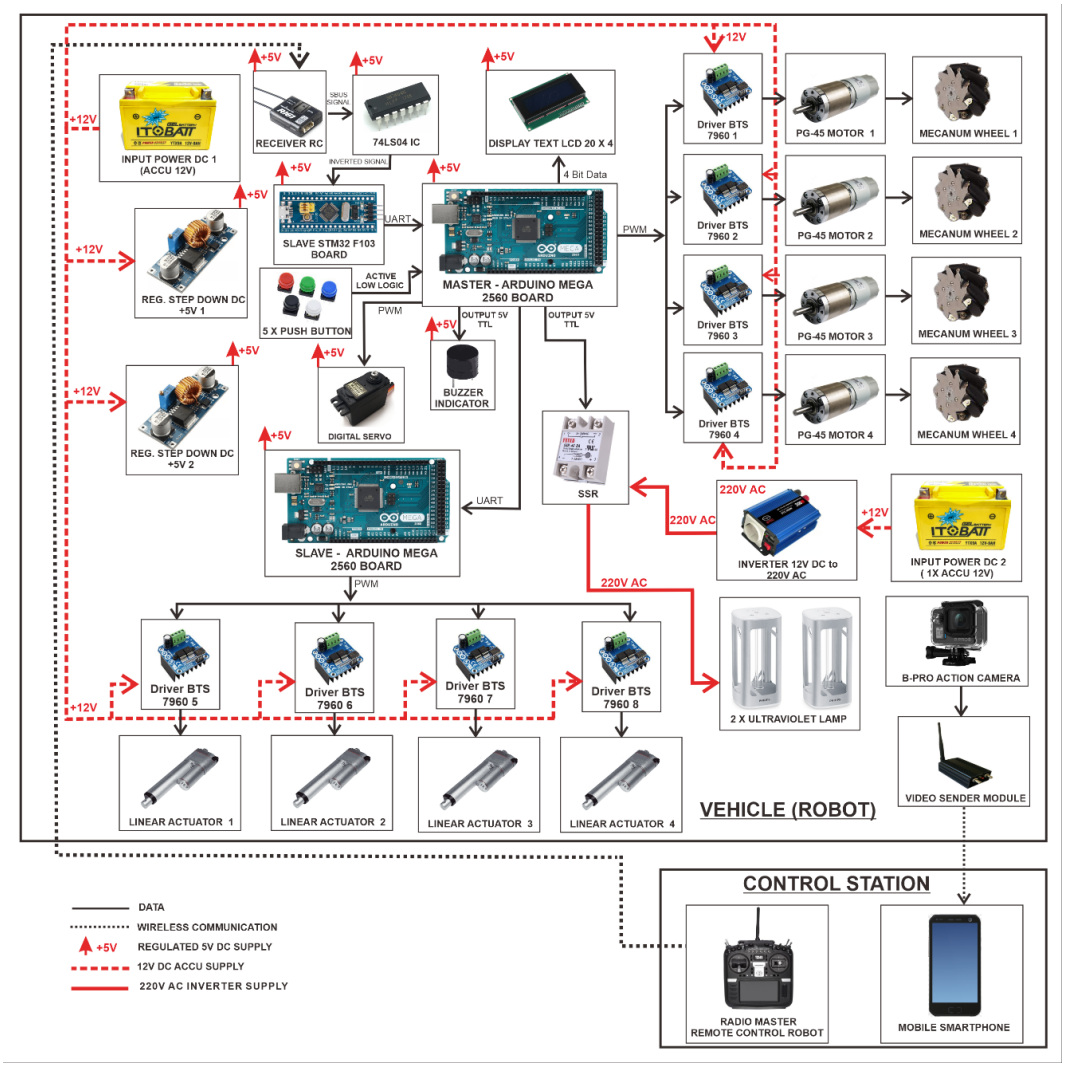

Figure 2: System block diagram.

3.2 Mechanical Design of the Manipulator

Mechanically, the disinfection arm is implemented as an articulated linkage structure providing three degrees of freedom (3-DoF). The motion is generated primarily by four linear actuators, which collectively implement the three joint motions required to orient the UV-C lamps toward targeted surfaces, as shown in Figure 3.

A key mechanical requirement is the ability to carry and position the actual UV-C disinfection equipment. The prototype was equipped with two functional PHILIPS UVC Disinfection Desk Lamps mounted near the end-effector. Each lamp has a mass of 0.812 kg, resulting in a total operational UV-C payload of 1.624 kg. Unless otherwise stated, the

experimental actuator-voltage, travel-time, joint-angle, and vertical-reach measurements reported in this study were obtained with both UV-C lamps installed.

To support operational flexibility, the manipulator implements an independent movement concept, allowing each arm segment/joint to be controlled individually. This mechanism allows the operator to adjust posture locally to reduce shadowed areas and to improve irradiation coverage in cluttered spaces.

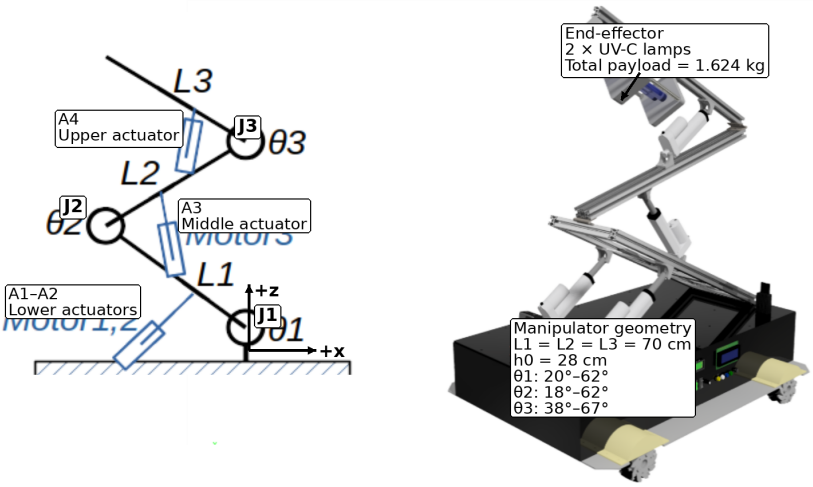

Figure 3: Mechanical and kinematic configuration of the proposed 3-DoF UV-C robotic manipulator. J1–J3 denote the rotational joints, A1–A4 denote the four linear actuators, and the coordinate frame is defined at J1 with the x- and z-axes representing the horizontal and vertical directions, respectively. The link lengths are $L_1 = L_2 = L_3 = 70$ cm, with a first-joint height offset of $h_0 = 28$ cm. The end-effector carries two functional UV-C lamps with a total payload of 1.624 kg.

3.3 Actuation and Motion Characteristics

The arm is driven by linear actuators, and motion commands from the wireless controller are translated into actuator extension/retraction commands by the embedded controller. The system utilizes four linear actuators to achieve 3-DoF arm motion, with wireless command data processed by an ATmega2560-based controller.

To characterize actuation performance, the proposed system uses timing measurements for actuator strokes from minimum to maximum and from maximum to minimum. The measured average stroke times indicate actuation dynamics on the order of 14–16 seconds, depending on the actuator position (lower/middle/upper), as shown in Figure 4 and Figure 5. These timing characteristics are important for the design of the teleoperation because they define how quickly the UV-C source can be repositioned during a disinfection routine.

Changes in actuator length directly affect joint angles. The joint-angle ranges from Joint 1 to Joint 3 were measured using an inclinometer app, and the minimum and maximum angles were recorded for the two extreme actuator-length conditions. In addition, the reach-

able height of the end-effector relative to the ground was measured under the same extreme configurations to provide a practical indication of the vertical workspace during operation.

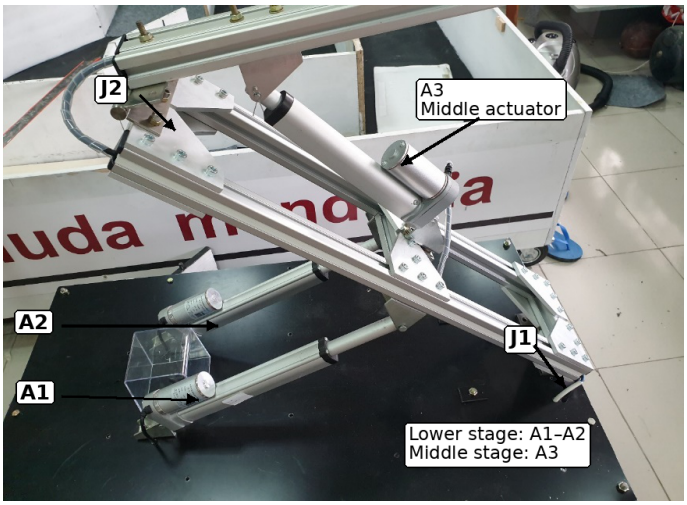

Figure 4: Annotated view of the lower and middle sections of the manipulator, showing lower linear actuators A1–A2, middle actuator A3, and Joints J1 and J2.

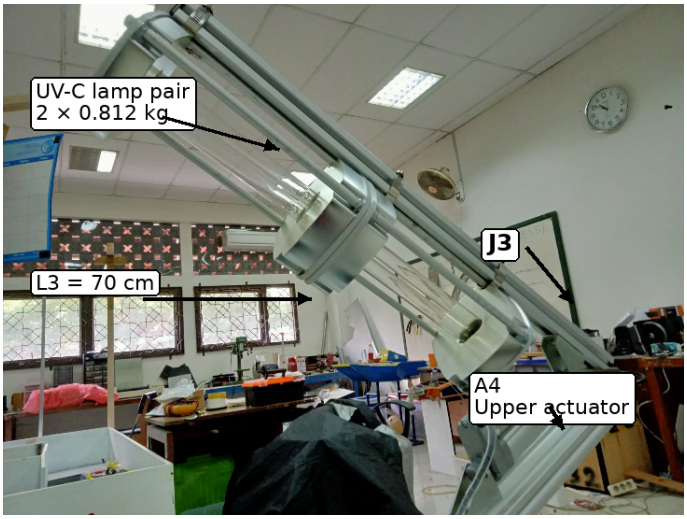

Figure 5: Annotated upper section of the manipulator showing Joint J3, upper linear actuator A4, the 70-cm upper link L_3, and the dual UV-C lamp payload.

3.4 Embedded Control and Motor Driver Layer

At the electronics level, arm movement is controlled by a central controller based on the ATmega2560 microcontroller platform, shown in Figure 6. Actuator power amplification is implemented using BTS7960 motor driver modules, which are selected for their high-current capability of up to 40 A. This driver selection aligns with the need to handle transient loads during actuator starts and reversals, and during operation under the structural and payload weight of the manipulator.

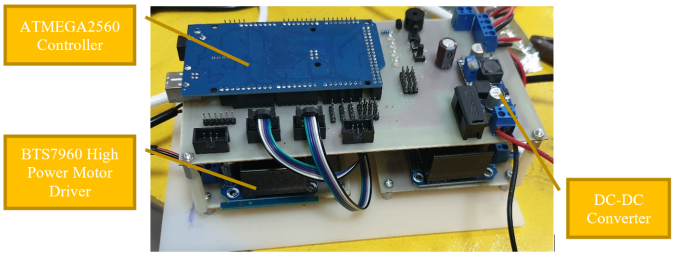

Figure 6: Embedded control and motor driver layer.

The actuator driver outputs were electrically validated while the arm operated under load. The measured output voltages show a modest drop from the no-load state (12.6 V) to the operating state (approximately 12.0–12.2 V), indicating that the power and driver layers can sustain actuator motion with limited voltage sag.

3.5 Power System and Teleoperation Support Components

The mobile robot platform is powered by two 12-V, 12-Ah valve-regulated lead-acid (VRLA) batteries connected in series. Specifications of the VRLA batteries and series-connected battery pack shown in Table 1. Each battery has approximate physical dimensions of $15 \times 9.8 \times 9.8$ cm and a mass of 4.17 kg. Accordingly, the complete battery pack provides a nominal voltage of 24 V and a capacity of 12 Ah, with a total battery mass of 8.34 kg. Since the batteries are connected in series, the voltage of the battery pack is doubled while the nominal ampere-hour capacity remains unchanged. The corresponding nominal stored energy is

$$E_{\mathrm{bat}} = V_{\mathrm{bat}} C_{\mathrm{bat}}, \tag{1}$$

where V_{bat} and C_{bat} denote the nominal battery-pack voltage and capacity, respectively. For the battery configuration used in this study,

$$E_{\mathrm{bat}} = 24 \times 12 = 288 \text{ Wh}. \tag{2}$$

The battery pack is installed in the lower section of the mobile robot chassis. This placement increases the total mass of the platform but also contributes to lowering the overall center of gravity, which is beneficial for static stability when the robotic manipulator is extended. Nevertheless, the additional 8.34-kg battery mass increases the inertial load that must be accelerated and decelerated by the mobile platform. Consequently, battery weight

can influence acceleration, braking response, turning behavior, and the torque required from the drive motors. To support teleoperation and situational awareness, the proposed system uses an HDMI wireless video transceiver (Hollyland MARS 300 Pro), indicating the design intent to provide remote visual feedback during operation.

Table 1: Specifications of the VRLA batteries and series-connected battery pack.

Specification	Individual Battery	Two-Battery Pack
Nominal voltage	12 V	24 V
Capacity	12 Ah	12 Ah
Nominal energy	144 Wh	288 Wh
Dimensions	$15 \times 9.8 \times 9.8$ cm	Two units
Terminal type	F2 (T2)	F2 (T2)
Mass	4.17 kg	8.34 kg

3.6 Integration with the Mobile Robot Platform

The disinfection arm is designed to function as a subsystem of a complete mobile UV-C disinfection robot. The arm is integrated with a mobile robot to form a complete UV-C disinfection robot system. The final prototype was assembled in this configuration, with the arm mounted on a mobile base. For the mobile base, PG56-class DC motors rated at 36 kgf·cm were used to support the integrated system concept for indoor deployment.

4 Results and Discussion

4.1 Prototype realization and integration

A full-scale prototype of the UV-C disinfection robotic manipulator was successfully fabricated and integrated on a mobile robot platform, forming a complete UV-C disinfection robot system. The realized platform demonstrates the intended configuration, in which a multi-link arm carries UV-C lamps at the end effector and can be positioned to illuminate target surfaces while the mobile base remains at a safe distance.

4.2 Battery mass and its impact on mobile-platform performance

The two VRLA batteries contribute a combined mass of 8.34 kg to the mobile robot platform. Therefore, the battery system represents a non-negligible portion of the robot mass and must be considered when evaluating the mobility and stability of the integrated platform.

From a mobility perspective, increasing the robot mass increases the traction force and motor torque required during acceleration, deceleration, and turning. The battery mass may therefore reduce the achievable acceleration and increase the response time of the mobile platform compared with an unloaded chassis. However, the battery pack is located near the bottom of the robot chassis, which lowers the center of gravity and improves resistance to overturning when the UV-C manipulator is extended away from the mobile-

platform centerline. Thus, the selected battery arrangement introduces a trade-off between mobility and static stability.

The nominal energy capacity of the battery pack is 288 Wh. The ideal operating time can therefore be estimated from

$$t_{\text{ideal}} = \frac{E_{\text{bat}}}{P_{\text{avg}}}, \tag{3}$$

where P_{avg} is the average electrical power consumed by the mobile base, manipulator actuators, control electronics, and UV-C equipment. In practice, the usable operating time is lower than the theoretical value because of battery discharge characteristics, actuator peak-current demand, conversion losses, and the operating duty cycle. Therefore, the present battery capacity should be interpreted as a nominal energy specification rather than a directly measured operating-time value.

4.3 Electrical performance of linear-actuator driving stage

To evaluate the actuator driving stage under a realistic disinfection payload, the measurements were performed while two functional PHILIPS UVC Disinfection Desk Lamps were installed on the manipulator. Each lamp has a mass of 0.812 kg, resulting in a total UV-C payload of 1.624 kg. Therefore, the reported operating-voltage measurements represent the fully loaded operational configuration rather than an unloaded manipulator. The measured supply voltage was 12.6 V under idle conditions and decreased to 12.0–12.2 V during actuator movement, corresponding to a voltage drop of 0.4–0.6 V depending on the actuator location, as shown in Table 2. These results indicate that the selected driver architecture can maintain near-nominal voltage under load, suggesting adequate electrical headroom for arm motion during UV disinfection operations.

Table 2: Measured voltage at the linear-actuator driver outputs with the full 1.624-kg UV-C payload (idle vs. operating).

No.	Linear Actuator	Idle (V)	Operating (V)	Drop (V)
1	Lower Actuator 1	12.6	12.0	0.6
2	Lower Actuator 2	12.6	12.0	0.6
3	Middle Actuator	12.6	12.2	0.4
4	Upper Actuator	12.6	12.2	0.4

4.4 Dynamic response: actuator travel time

The actuator travel-time measurements were also conducted with the complete 1.624-kg UV-C payload installed. Timing tests were conducted to characterize the actuation speed from the minimum stroke to the maximum stroke (extension) and from the maximum stroke to the minimum stroke (retraction). Three repeated trials were recorded for each actuator group and summarized as average timing values, as shown in Table 3. The measured average travel times are:

- Lower: 16.29 s (min→max) and 16.32 s (max→min)

- Middle: 15.34 s (min→max) and 15.80 s (max→min)
- Upper: 14.70 s (min→max) and 14.74 s (max→min)

Overall, the arm demonstrates consistent motion timing across repeated trials, which is important for predictable remote operation and repeatable UV pointing during disinfection tasks.

Table 3: Linear-actuator stroke timing measurements with the full 1.624-kg UV-C payload.

Linear Actuator	Length Status	Timing Measurements (s)			Average (s)
		1	2	3	
Lower Linear Actuator	Min to Max	16.44	16.31	16.11	16.28667
	Max to Min	16.42	16.36	16.19	16.32333
Middle Linear Actuator	Min to Max	15.65	15.32	15.05	15.34
	Max to Min	15.90	16.00	15.50	15.80
Upper Linear Actuator	Min to Max	14.72	14.70	14.63	14.70833
	Max to Min	14.85	14.69	14.68	14.74

4.5 Kinematic range: joint angle variation

The effect of actuator stroke on arm posture was evaluated by measuring inter-link tilt angles with an inclinometer app on an Android smartphone. The joint-angle ranges reported in Table 4 were measured with both UV-C lamps installed and therefore represent the achievable angular workspace under full operational payload. Measurements were taken at two boundary conditions: when all linear actuators were at minimum stroke and when all were at maximum stroke. The range of arm movement is shown in Figure 7.

The observed joint-angle ranges were Joint 1: (20 °) to (62°), Joint 2: (18°) to (62°), and Joint 3: (38°) to (67°). This range confirms that the 3-DoF configuration can generate multiple irradiation postures, supporting the goal of steering UV light toward complex surfaces and reducing shadowed regions.

Table 4: Measured joint-angle ranges under the full 1.624-kg UV-C payload at extreme actuator-length conditions.

All Linear Actuators	Joint Angles (°)		
	θ_1	θ_2	θ_3
Minimum	20	18	38
Maximum	62	62	67

4.6 End-effector vertical reach

The end-effector height was measured from the wheel-ground plane to the highest point of the arm tip in two boundary configurations with all actuators at minimum stroke and all at

maximum stroke, as summarized in Table 5. The measured vertical reach spans 129.5–224 cm, demonstrating that the mechanism can address both lower and higher target areas typically encountered in indoor environments (e.g., bed rails, cabinet faces, and wall surfaces).

Table 5: End-effector height relative to ground at extreme actuator-length conditions

All Linear Actuators	End-Effector Height Relative to Ground (cm)
Minimum	224.0
Maximum	129.5



Figure 7: Experimentally demonstrated manipulator configurations.The two larger images show representative boundary configurations, while the remaining images illustrate intermediate arm postures. The measured joint ranges were $20°$–$62°$, $18°$–$62°$, and $38°$–$67°$ for J1–J3, respectively, with a measured end-effector height range of 129.5–224 cm.

4.7 Forward Kinematics-Based Workspace Estimation and Visualization

To support workspace evaluation both analytically and visually, a forward kinematics model was developed for the 3-DoF articulated manipulator. Since the manipulator mainly operates in a vertical plane to position the UV-C lamps at different heights and irradiation angles, the arm was approximated as a planar serial-link mechanism. The base coordinate frame was defined at the first joint, with the horizontal and vertical axes denoted by x and z, respectively. The lengths of the link were defined as L_1, L_2 and L_3, while the height offset of the first joint from the ground was denoted by h_0. In this model, the measured angles were treated as relative joint angles in the vertical plane.

The forward kinematics equations of the end-effector are expressed as:

$$x_e = L_1 \cos\theta_1 + L_2 \cos(\theta_1 + \theta_2) + L_3 \cos(\theta_1 + \theta_2 + \theta_3) \tag{4}$$

$$z_e = h_0 + L_1 \sin\theta_1 + L_2 \sin(\theta_1 + \theta_2) + L_3 \sin(\theta_1 + \theta_2 + \theta_3) \tag{5}$$

$$\phi_e = \theta_1 + \theta_2 + \theta_3 \tag{6}$$

where x_e and z_e represent the horizontal and vertical positions of the UV-C lamp/end-effector, respectively, and ϕ_e represents the end-effector orientation. In this study, the link lengths were $L_1 = 70$ cm, $L_2 = 70$ cm, and $L_3 = 70$ cm, while the first-joint height offset was $h_0 = 28$ cm.

Using the experimentally measured joint-angle ranges in Table 4, namely $\theta_1 = 20°$–$62°$, $\theta_2 = 18°$–$62°$, and $\theta_3 = 38°$–$67°$, the estimated planar workspace was calculated by varying the joint angles within these limits. For each joint-angle combination, the corresponding end-effector position (x_e, z_e) was computed using the forward kinematics equations and plotted to form the estimated workspace envelope.

The simulation results showed that the end-effector could reach a horizontal position of approximately -76.3 cm to 137.9 cm relative to the first joint and a vertical position of approximately 134.5 cm to 220.5 cm from the ground. The corresponding end-effector orientation ranged from $76°$ to $191°$.

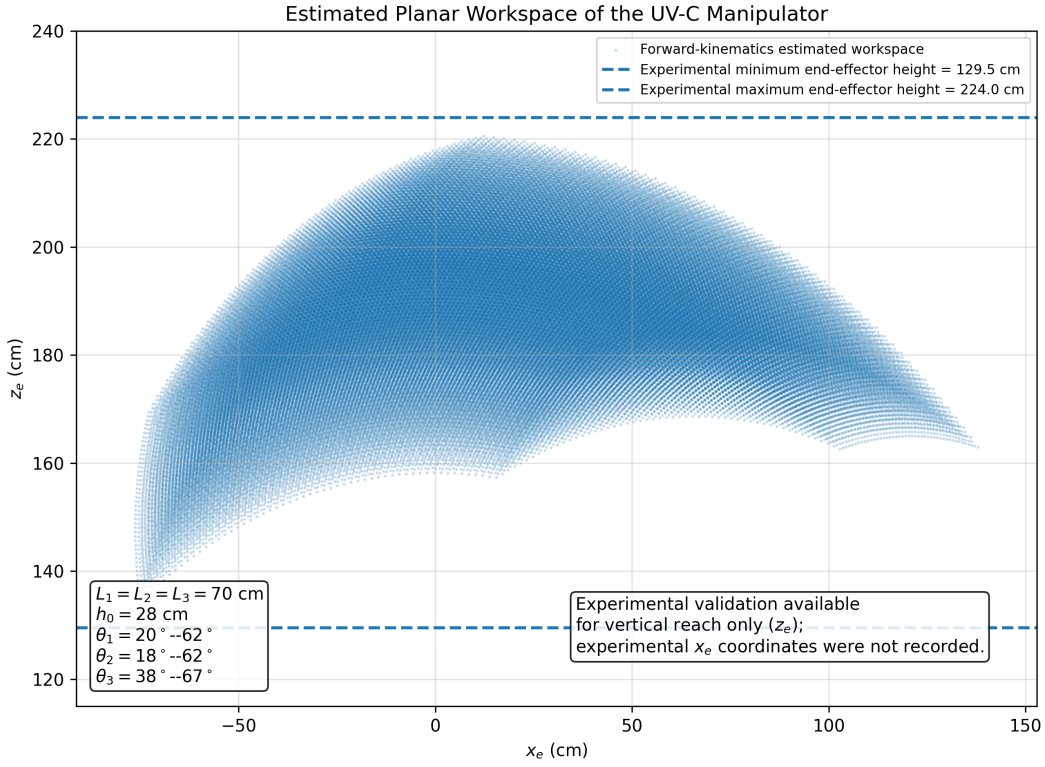

Figure 8: Forward-kinematics-based planar workspace of the UV-C manipulator using $L_1 = L_2 = L_3 = 70$ cm, $h_0 = 28$ cm, and the experimentally measured joint-angle limits. The dashed horizontal lines indicate the experimentally measured minimum and maximum end-effector heights of 129.5 cm and 224.0 cm, respectively.

The resulting workspace, shown in Figure 8, provides a visual representation of the reachable region of theUV-C end-effector in the vertical plane. The forward-kinematicsmodel was constructed using three equal link lengths of $L_1 = L_2 = L_3 = 70$ cm, a first-joint height offset of $h_0 = 28$ cm,and the experimentally measured joint-angle limits.The estimated workspace extends from approximately -76.3 to 137.9 cm in the horizontal direction and from 134.5 to 220.5 cm in the vertical direction. Experimental measurements performed at the two extreme actuator configurations resulted in end-effector heights of 129.5 and 224.0 cm. These experimentally measured vertical limits have been overlaid on the revised workspace figure to provide a direct comparison between the analytical predictionand the physical prototype.

The analytical and experimental vertical ranges are in reasonable agreement. The differences of approximately 5 cm at the lower boundary and 3.5 cm at the upper boundary can be attributed to mechanical offsets, joint clearances, the UV-C lamp mounting structure, measurement uncertainty, and the simplification of the physical manipulator into an ideal planar serial-link model.

It should be noted that the original experimental measurements recorded the end-effector height relative to the ground but did not record the corresponding horizontal coordinate x_e. Therefore, the current comparison validates the vertical extent of the predicted workspace rather than providing point-by-point experimental validation over the complete x_e–z_e plane.

The generated workspace should be interpreted as an estimated kinematic workspace based on the allowable joint-angle ranges. Since the angle limits were derived from experimental boundary measurements, the plot represents a workspace envelope rather than complete evidence that all angle combinations are physically achievable under every mechanical configuration. Therefore, the forward kinematics analysis and workspace visualization support the experimental finding that the proposed manipulator provides a practical workspace for directing UV-C irradiation toward both lower and higher indoor target surfaces.

4.8 Functional validation with UV-C payload

Prototype testing confirms that the arm is capable of carrying and orienting two UV-C lamps during operation, as shown in Figure 9. The actuators can lift the UV-C payload and direct it to the desired location, and the 3-DoF arm enables reaching the irradiation angles required for room-disinfection scenarios.

4.9 Payload-Dependent Load Analysis

To clarify the operational load condition of the proposed manipulator, the UVC lamps employed in this study were not dummy loads but two functional Philips UVC Disinfection Desk Lamps. Each lamp has a mass of 0.812 kg, resulting in a total operational payload of 1.624 kg. Therefore, the gravitational force associated with the complete UV-C payload is approximately 15.93 N.

A quasi-static payload analysis was performed to quantify the additional mechanical loading imposed by the UV-C equipment. Three payload conditions were considered: no lamp ($P_0 = 0$ kg), one UV-C lamp ($P_1 = 0.812$ kg), and two UV-C lamps ($P_2 = 1.624$ kg).

The latter represents the actual configuration used during the experimental evaluation of the prototype.

Assuming that the UV-C payload is concentrated near the end-effector, the additional gravitational moments acting on the three joints can be expressed as

$$\tau_1 = m_p g \left[L_1 \cos\theta_1 + L_2 \cos(\theta_1 + \theta_2) + L_3 \cos(\theta_1 + \theta_2 + \theta_3) \right], \tag{7}$$

$$\tau_2 = m_p g \left[L_2 \cos(\theta_1 + \theta_2) + L_3 \cos(\theta_1 + \theta_2 + \theta_3) \right], \tag{8}$$

and

$$\tau_3 = m_p g L_3 \cos(\theta_1 + \theta_2 + \theta_3), \tag{9}$$

where m_p is the payload mass and $g = 9.81\ \mathrm{m/s^2}$. The link lengths used in the analysis were $L_1 = L_2 = L_3 = 0.70$ m, consistent with the forward-kinematics model.

The joint angles were varied throughout the experimentally measured ranges of $\theta_1 = 20°$–$62°$, $\theta_2 = 18°$–$62°$, and $\theta_3 = 38°$–$67°$. The maximum absolute payload-induced gravitational moments obtained from the simulation are summarized in Table 6.

Table 6: Maximum absolute payload-induced gravitational moments over the measured joint-angle ranges

Payload Condition	Mass (kg)	$\max\lvert\tau_1\rvert$ (N·m)	$\max\lvert\tau_2\rvert$ (N·m)	$\max\lvert\tau_3\rvert$ (N·m)
P_0: no lamp	0	0	0	0
P_1: one lamp	0.812	10.98	8.69	5.58
P_2: two lamps	1.624	21.97	17.39	11.15

As expected, the additional gravitational loading increased approximately linearly with the UV-C payload. With both lamps installed, the maximum payload-induced moments were approximately 21.97 Nm, 17.39 Nm, and 11.15 Nm at Joints 1, 2, and 3, respectively. The largest moment at Joint 1 occurred when the manipulator was extended toward the forward region of its workspace, where the horizontal distance between the payload and the first joint was greatest.

It should be emphasized that these values represent only the additional gravitational moments generated by the UV-C payload; the masses of the links, actuators, and mounting structures are not included in the quasi-static model. Nevertheless, the analysis provides a quantitative indication of the additional mechanical demand associated with the actual disinfection equipment.

Importantly, the experimental measurements reported in the previous subsections were performed with both operational UV-C lamps installed, corresponding to the full payload condition $P_2 = 1.624$ kg. Under this condition, the manipulator achieved joint ranges of $20°$–$62°$, $18°$–$62°$, and $38°$–$67°$ for Joints 1–3, respectively, while maintaining an end-effector vertical reach of 129.5–224 cm. The actuator driver voltage remained between 12.0 and 12.2 V during movement, and no actuator stall or loss of motion was observed. These results demonstrate that the manipulator remains functional throughout the tested workspace while carrying the complete 1.624-kg operational UV-C payload.

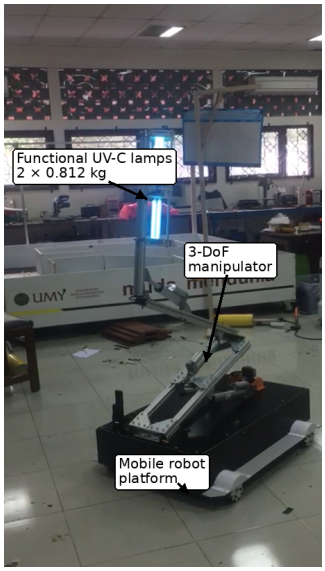

Figure 9: Integrated UV-C disinfection robotic platform showing the functional dual UV-C lamps, 3-DoF robotic manipulator, and mobile robot base during operation.

4.10 Simulation-Based Shadow-Region Accessibility Analysis

To quantitatively evaluate the geometric capability of the proposed manipulator to mitigate shadowed regions, a two-dimensional line-of-sight simulation was performed. The purpose of this analysis was not to repeat the biological UV-C effectiveness experiment reported in our previous study [21], but rather to assess the specific robotic contribution of repositioning the UV-C source relative to geometrically occluded target surfaces.

The simulation used the experimentally characterized manipulator parameters reported in this study. The link lengths were $L_1 = L_2 = L_3 = 70$ cm, and the first-joint height offset was $h_0 = 28$ cm. The joint variables were constrained to the measured ranges of $\theta_1 = 20°$–$62°$, $\theta_2 = 18°$–$62°$, and $\theta_3 = 38°$–$67°$.

A vertical target surface was defined at $x = 155$ cm and sampled over the height range $z = 135$–225 cm. To represent a typical occluding object in an indoor healthcare environment, an opaque rectangular obstacle was placed between the source and the target, spanning $x = 95$–135 cm and $z = 155$–195 cm. Two irradiation configurations were evaluated: (1) a fixed-source configuration with the UV-C source located at $(20, 170)$ cm, representing a conventional static UV-C setup, and (2) a manipulator-repositioned configuration in which the source could be moved within the reachable manipulator workspace subject to a conservative collision-safe constraint ($x \leq 95$ cm), thereby keeping the source on the robot side of the obstacle.

For each target point P_i, a visibility indicator was defined as

$$V_i = \begin{cases} 1, & \text{if the source-to-target path is unobstructed,} \\ 0, & \text{if the path intersects the obstacle.} \end{cases} \tag{10}$$

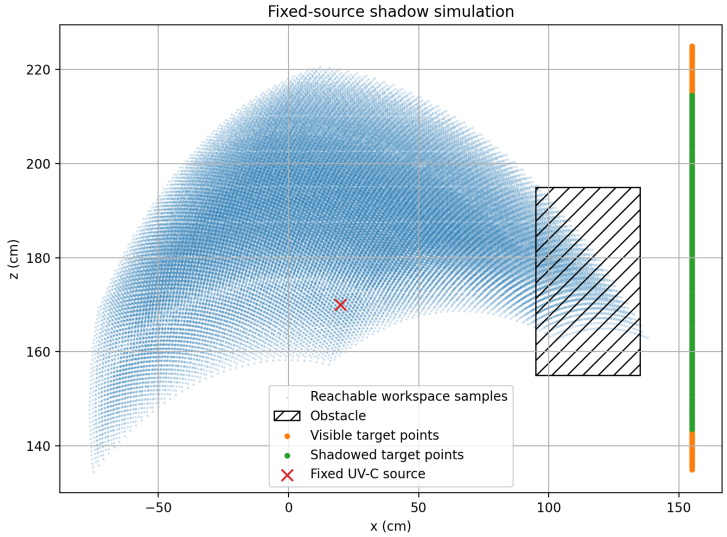

Figure 10: Geometry-based shadow simulation for the fixed-source UV-C configuration. The obstacle blocks direct line-of-sight to a large portion of the target surface, resulting in limited geometric coverage.

For the fixed-source configuration, visibility was evaluated from the single static source position. For the manipulator-repositioned configuration, $V_i = 1$ when at least one collision-safe reachable source pose provided an unobstructed path to target point P_i. The geometric irradiation coverage was then calculated as

$$C = \frac{1}{N} \sum_{i=1}^{N} V_i \times 100\%, \tag{11}$$

where N is the number of sampled target points. The corresponding shadowed-area fraction is

$$S = 100\% - C. \tag{12}$$

To quantify the improvement obtained by source repositioning, the shadow-reduction ratio was defined as

$$SR = \frac{S_{\text{fixed}} - S_{\text{manip}}}{S_{\text{fixed}}} \times 100\%. \tag{13}$$

The simulation results show that the fixed-source configuration provided a geometric coverage of 20.99%, leaving 79.01% of the evaluated target region shadowed, as shown in Figure 10. When the UV-C source was repositioned using the articulated manipulator, the accessible geometric coverage increased to 62.98%, while the shadowed fraction decreased to 37.02%, as shown in Figure 11. This corresponds to an absolute coverage gain of 41.99 percentage points and a shadow-reduction ratio of 53.15%.

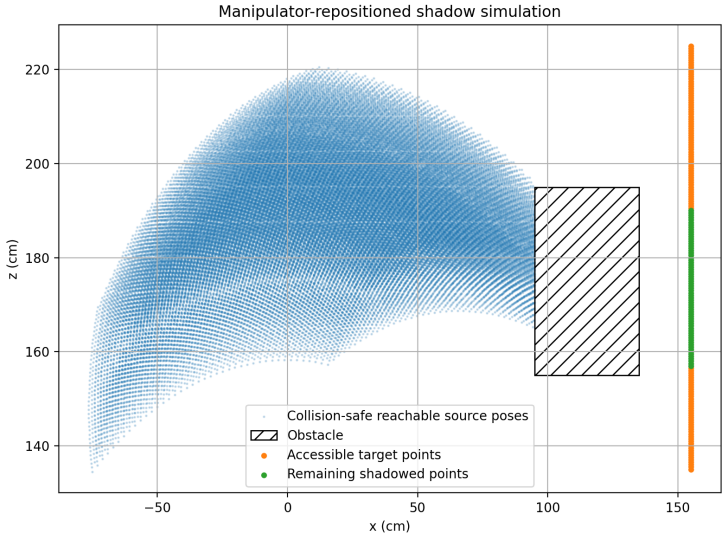

Figure 11: Geometry-based shadow simulation for the manipulator-repositioned UV-C configuration. By repositioning the source within the reachable workspace, the articulated manipulator increases line-of-sight access to previously shadowed target regions.

These results provide quantitative evidence that the proposed manipulator can improve line-of-sight accessibility to surfaces that would otherwise remain shadowed in a fixed-source UV-C configuration. It should be emphasized, however, that this simulation evaluates geometric accessibility only and does not directly represent absolute UV-C irradiance, delivered UV dose, or microbial inactivation. Direct radiometric and microbiological validation of the integrated robotic platform remains a subject for future work.

4.11 Limitations

The results validate the feasibility of a linear-actuator-driven manipulator for UV disinfection, particularly in remote operations where human exposure to UV radiation must be minimized. However, the current evaluation focuses on electromechanical performance, including voltage drop, travel time, reachable posture and height, and quasi-static payload-induced gravitational moments. Quantitative disinfection efficacy (e.g., delivered UV dose, exposure uniformity, and microbial inactivation tests) is not yet reported and should be conducted in future work to strengthen claims for hospital deployment. Future mechanical validation should also measure actuator force and total joint loading under dynamic motion, including the effects of link self-weight, acceleration, friction, and structural compliance. In addition, the effect of varying UV-C payloads on end-effector positioning accuracy, mobile-platform maneuverability, and dynamic stability was not experimentally quantified in the present study and should be investigated in future work.

The shadow-region analysis presented in this study is geometry-based and therefore quantifies line-of-sight accessibility rather than absolute UV-C irradiance, delivered dose, or microbial inactivation. Although the biological effect of UV irradiation was investigated

experimentally in our previous study [21], direct radiometric validation of the integrated manipulator system under realistic operating conditions remains necessary.

5 Conclusion

This study presented the design, fabrication, and prototype-level evaluation of a UV-C disinfection robotic manipulator intended to support safer hospital disinfection by enabling remote operation and improved UV-C beam positioning in complex indoor environments. The developed system was realized as a 3-DoF articulated arm driven by linear actuators and integrated with a mobile robot platform, forming a complete disinfection robot configuration.

Experimental evaluation focused on the electromechanical performance and reachable workspace of the manipulator while carrying two UV-C lamps. Electrical testing revealed that the actuator driver output remained close to the nominal supply voltage, decreasing from 12.6 V under idle conditions to 12.0–12.2 V during motion, indicating that the power and driver stage can sustain arm operation under load. The actuator dynamic response was characterized through stroke-timing tests, yielding average travel times of 14.70–16.32 seconds, depending on the actuator position, with consistent behavior across repeated trials. Kinematic measurements confirmed practical posture variation, with joint-angle ranges of Joint 1 = 20°–62°, Joint 2 = 18°–62°, and Joint 3 = 38°–67°, demonstrating the ability to steer the UV-C payload toward different target directions. The arm also achieved a measured vertical reach of 129.5–224 cm at the end-effector, which is sufficient to address a wide range of typical indoor surface heights. The two functional UV-C lamps produced an operational payload of 1.624 kg. The quasi-static analysis estimated maximum absolute payload-induced moments of 21.97, 17.39, and 11.15 N·m at Joints 1, 2, and 3, respectively. The line-of-sight simulation further showed that manipulator-based source repositioning increased geometric target coverage from 20.99% to 62.98% and reduced the shadowed fraction by 53.15% relative to the fixed-source configuration.

In addition to experimental measurements, the forward kinematics-based workspace estimation provided analytical support for the observed workspace. The estimated planar workspace showed a horizontal reach of approximately -76.3–137.9 cm relative to the first joint and a vertical reach of approximately 134.5–220.5 cm from the ground, which is consistent with the measured end-effector height. Overall, the prototype testing and workspace analysis verify that the manipulator can carry and orient dual UV-C lamps and can be positioned across multiple configurations required for indoor disinfection tasks.

Despite these promising results, the current work primarily validates mechanical functionality and basic performance metrics. Future work should include quantitative UV dose mapping, irradiation uniformity analysis, and microbiological inactivation experiments to directly assess the effectiveness of disinfection in realistic hospital-room scenarios. In addition, improvements in motion speed, the inclusion of position feedback for closed-loop control, and higher-level coverage planning for coordinated base arm motion would further enhance operational reliability and reduce the likelihood of shadowed regions. The proposed UV-C disinfection robotic manipulator thus provides a feasible foundation for safer and more adaptable disinfection systems and can be extended toward more autonomous, clinically robust solutions.

Acknowledgments

The authors express their gratitude to the Molecular Medicine and Therapy Laboratory, Universitas Muhammadiyah Yogyakarta, for providing the necessary facilities. We also thank Universitas Muhammadiyah Yogyakarta for funding this research through the Research and Innovation Institute (LRI) under the 2020/2021 fiscal year research grant.

References

[1] M. Javaid, A. Haleem, R. Vaishya, S. Bahl, R. Suman, and A. Vaish, "Industry 4.0 technologies and their applications in fighting COVID-19 pandemic," *Diabetes & Metabolic Syndrome: Clinical Research & Reviews*, vol. 14, no. 4, pp. 419–422, 2020.

[2] R. R. Murphy, V. B. M. Gandudi, and J. Adams, "Applications of robots for COVID-19 response." arXiv preprint, 2020. arXiv:2008.06976.

[3] Y. Shen, D. Guo, F. Long, L. A. Mateos, H. Ding, Z. Xiu, R. B. Hellman, A. King, S. Chen, C. Zhang, and H. Tan, "Robots under COVID-19 pandemic: A comprehensive survey," *IEEE Access*, vol. 9, pp. 1590–1615, 2021.

[4] D. Feil-Seifer, K. S. Haring, S. Rossi, A. R. Wagner, and T. Williams, "Where to next? the impact of COVID-19 on human–robot interaction research," *ACM Transactions on Human-Robot Interaction*, vol. 10, no. 1, 2020.

[5] C. Esterwood and L. Robert, "Robots and COVID-19: Re-imagining human-robot collaborative work in terms of reducing risks to essential workers," *ROBONOMICS: The Journal of the Automated Economy*, vol. 1, p. 9, 2021.

[6] I. Mehta, H.-Y. Hsueh, S. Taghipour, W. Li, and S. Saeedi, "Uv disinfection robots: A review," *Robotics and Autonomous Systems*, vol. 161, p. 104332, 2023.

[7] D. Conte, S. Leamy, and T. Furukawa, "Design and map-based teleoperation of a robot for disinfection of COVID-19 in complex indoor environments," in *2020 IEEE International Symposium on Safety, Security, and Rescue Robotics (SSRR)*, pp. 276–282, 2020.

[8] M. Guettari, I. Gharbi, and S. Hamza, "UVC disinfection robot," *Environmental Science and Pollution Research*, vol. 28, no. 30, pp. 40394–40399, 2021.

[9] I. Chio, K. Ruan, Z. Wu, K. I. Wong, L. M. Tam, and Q. Xu, "Design and autonomous navigation of a new indoor disinfection robot based on disinfection modeling," *IEEE transactions on automation science and engineering*, vol. 20, no. 1, pp. 649–661, 2022.

[10] A. Zaman, M. S. Majib, S. A. Tanjim, S. M. A. Siddique, S. Islam, M. S. Aadeeb, N. I. Khan, R. Haque, M. R. U. Islam, M. R. F. Faisal, S. Malik, and M. N. Islam, "UVC-PURGE: A novel cost-effective disinfection robot for combating COVID-19 pandemic," *IEEE Access*, vol. 10, pp. 37613–37634, 2022.

[11] N. Mikhailovskiy, A. Sedunin, S. Perminov, I. Kalinov, and D. Tsetserukou, "UltraBot: Autonomous mobile robot for indoor UV-C disinfection," in *2021 IEEE 17th International Conference on Automation Science and Engineering (CASE)*, pp. 2147–2152, 2021.

[12] J. M. C. Marques, R. Ramalingam, Z. Pan, and K. Hauser, "Optimized coverage planning for UV surface disinfection," in *2021 IEEE International Conference on Robotics and Automation (ICRA)*, pp. 9731–9737, 2021.

[13] J. Conroy, C. Thierauf, P. Rule, E. A. Krause, H. A. Akitaya, A. Gonczi, M. Korman, and M. Scheutz, "Robot development and path planning for indoor ultraviolet light disinfection," in *2021 IEEE International Conference on Robotics and Automation (ICRA)*, pp. 7795–7801, 2021.

[14] A. G. Sanchez and W. D. Smart, "Verifiable surface disinfection using ultraviolet light with a mobile manipulation robot," *Technologies*, vol. 10, no. 2, p. 48, 2022.

[15] I. Mehta, H.-Y. Hsueh, N. Kourtzanidis, M. Brylka, and S. Saeedi, "Far-uvc disinfection with robotic mobile manipulator," in *2022 International Symposium on Medical Robotics (ISMR)*, pp. 1–8, 2022.

[16] C. Zhang, H. Qin, S. Sun, Y. Pan, K. Liu, T. Li, and X. Zhao, "Jpmdp: Joint base placement and multi-configuration path planning for 3d surface disinfection with a uv-c robotic system," *Robotics and Autonomous Systems*, vol. 174, p. 104644, 2024.

[17] P. Guo, D. Luo, Y. Wu, S. He, J. Deng, H. Yao, W. Sun, and J. Zhang, "Coverage planning for uvc irradiation: Robot surface disinfection based on swarm intelligence algorithm," *Sensors*, vol. 24, no. 11, p. 3418, 2024.

[18] K. Ruan, Z. Wu, and Q. Xu, "Smart cleaner: A new autonomous indoor disinfection robot for combating the COVID-19 pandemic," *Robotics*, vol. 10, no. 3, p. 87, 2021.

[19] M. Y. Mustar, B. S. Tryatmojo, R. Febrian, K. Purwanto, R. F. Siregar, *et al.*, "Design and implementation of a 2-dof manipulator based on inverse kinematics for agricultural robotic competition," in *2025 5th International Conference on Electronic and Electrical Engineering and Intelligent System (ICE3IS)*, pp. 131–136, IEEE, 2025.

[20] M. Y. Mustar, B. S. Tryatmojo, S. G. Kusuma, Y. K. M. Putra, H. A. Sasono, and R. O. Wiyagi, "Exploring the potential of intel realsense t265 camera as visual odometry and tracking system for autonomous navigation of four-wheel omnidirectional mobile robot," in *2024 4th International Conference on Electronic and Electrical Engineering and Intelligent System (ICE3IS)*, pp. 115–120, IEEE, 2024.

[21] A. Adiningrat, A. G. Fadhlurrahman, Y. Rismawanto, T. K. Hariadi, M. Ulfa, R. O. Wiyagi, and M. Y. Mustar, "The effects of UV light wavelength and distance differences in viral genetic material integrity," in *AIP Conference Proceedings*, vol. 3155, p. 060001, AIP Publishing, 2024.